Smooth Stress Relief of Trifluoroacetate Metal-Organic Solutions for $YBa_2Cu_3O_7$ Film Growth

Katerina Zalamova,* Neus Romà, Alberto Pomar, Stephanie Morlens, Teresa Puig, Jaume Gázquez, Anna E. Carrillo, Felip Sandiumenge, Susana Ricart, Narcís Mestres, and Xavier Obradors

Institut de Ciència de Materials de Barcelona, CSIC, Campus de la UAB, 08193 Bellaterra, Catalonia, Spain

Received July 6, 2006

The mechanisms controlling stress relief during the drying and pyrolysis processes of trifluoroacetate metal-organic precursors have been elucidated in view of high rate fabrication of epitaxial superconducting $YBa_2Cu_3O_7$ thin films. Combining FTIR, TGA, and film thickness evolution measurements, we conclude that gel drying and sintering occurs below $T \sim 250$ °C while film densification, due to metal-organic pyrolysis, occurs in the range 250−310 °C. Stress relief is the driving force leading to smooth or structurally inhomogeneous films, displaying buckling or macrocracks, depending on the rate of film transformation. High heating rates can be used during the gel drying and sintering process preserving the film homogeneity because the developed stress is below that required to generate buckling, as demonstrated by nanoindentation experiments. Within the temperature window where the metal-organic decomposition process occurs, the gas flow and the temperature ramp can be tuned to achieve fast pyrolysis preserving the film homogeneity. Optical microscopy, TEM, SEM, AFM, nanoindentation, μ-Raman spectroscopy, electrical resistivity, and critical current measurements of the films have been combined to stress the relevance of preserving the homogeneity of the films from the nanometric to the macroscopic length scales, to achieve high critical current $YBa_2Cu_3O_7$ thin films, i.e., $J_c \approx 3-4$ MA/cm^2 at 77 K.

I. Introduction

Chemical solution deposition (CSD) is a cost-effective technique with a high potential for preparation of functional large area and long length films.[1] Many oxides with electronic, electrical, ferroelectric, dielectric, magnetic, or superconducting functionalities have been prepared by CSD having either a polycrystalline or an epitaxial structure.[2−7] High-temperature superconducting coated conductors are one example where preparation of high-quality epitaxial thin films with long lengths is required and, therefore, CSD is a promising alternative to the conventional physical deposition techniques.[8−13] One of the challenges of the solution-based deposition processes, however, is to avoid the formation of microstructural inhomogeneities, which could influence their functionality, during any of the steps converting the deposited chemical solution into the crystalline film.[14−16] This process consists of one or two steps, depending on the compliance of the films during the densification, pyrolysis, and crystallization processes. In a single-step process the removal of the organic constituents and the oxide crystallization occur simultaneously while in the two-step process they are separately accomplished. Several characterizations of the metal-organic precursor chemistry (reactivity and decomposition temperature) and the complex rearrangement leading to amorphous or nanocrystalline phases resulting from the pyrolysis will determine the choice of a given process. Some ferroelectric oxides, for instance, can be prepared through a one-step rapid thermal annealing process (>100 °C/s) without formation of cracks or blisters.[2] Trifluoroacetate (TFA) metal-organic decomposition (MOD) has been largely investigated as a chemical solution route leading to high-quality $YBa_2Cu_3O_7$ (YBCO) superconducting films with high critical

* To whom correspondence should be addressed. E-mail: kzalamova@icmab.es.

(1) Shimoda, T.; Matsuki, Y.; Furusawa, M.; Auki, T.; Yudasaka, I.; Tanaka, H.; Iwasawa, H.; Wang, D.; Miyasaka, M.; Takeuchi, Y. *Nature* **2006**, *440*, 783.
(2) Schwartz, R. W. *Chem. Mater.* **1997**, *9*, 2325.
(3) Lange, F. F. *Science* **1996**, *273*, 903.
(4) Bhuiyan, M. S.; Paranthaman, M.; Salama, K. *Supercond. Sci. Technol.* **2006**, *19*, R1.
(5) Manabe, T.; Yamaguchi, I.; Kondo, W.; Mizuta, S.; Kumagai, T. *J. Mater. Res.* **1997**, *12*, 541.
(6) Jia, Q. X.; Mccleskey, T. M.; Burrell, A. K.; Lin, Y.; Collis, G. E.; Wang, H.; Li, A.D. Q.; Foltin, S. R. *Nat. Mater.* **2004**, *3*, 529.
(7) Schwartz, R. W.; Schneller, T.; Waser, R. *C. R. Chim.* **2004**, *7*, 433.
(8) Larbalestier, D.; Gurevich, A.; Feldmann, D. M.; Polyanskii, A. *Nature* **2001**, *414*, 369.
(9) Dawley, J. T.; Ong, R. J.; Clem, P. G. *J. Mater. Res.* **2002**, *17*, 1678.
(10) Sandiumenge, F.; Cavallaro, A.; Gázquez, J.; Puig, T.; Obradors, X.; Arbiol, J.; Freyhardt, H. C. *Nanotechnology* **2005**, *16*, 1809.
(11) Honjo, T.; Nakamura, Y.; Teranishi, R.; Tokunaga, Y.; Fuji, H.; Shibata, J.; Asada, S.; Izumi, T.; Shiohara, Y.; Ijima, Y.; Saitoh, T.; Kaneko, A.; Murata, K. *Physica C* **2003**, *392*−*396*, 873.
(12) Rupich, M. W.; Zhang, W.; Li, X.; Kodenkandath, T.; Verebelyi, D. T.; Schoop, U.; Thieme, C.; Teplitsky, M.; Lynch, J.; Nguyen, N.; Siegal, E.; Scudiere, J.; Maroni, V.; Venkataraman, K.; Miller, D.; Holesinger, T. G. *Physica C* **2004**, *412*−*414*, 877.
(13) Obradors, X.; Puig, T.; Pomar, A.; Sandiumenge, F.; Mestres, N.; Coll, M.; Cavallaro, A.; Roma, N.; Gazquez, J.; Gonzalez, J. C.; Castaño, O.; Gutierrez, J.; Palau, A.; Zalamova, K.; Morlens, S.; Hassini, A.; Gubert, M.; Ricart, S.; Moreto, J. M.; Piñol, S. *Supercond. Sci. Technol.* **2006**, *19*, S13.
(14) Takenaka, S.; Kozuka, H. *Appl. Phys. Lett.* **2001**, *79*, 3485.
(15) Park, G. T.; Choi, J. J.; Park, C. S.; Lee, J. W.; Kim, H. E. *Appl. Phys. Lett.* **2004**, *85*, 2322.
(16) Kozuka, H.; Kajimura, M.; Hirano, T.; Katayama, K. *J. Sol-Gel Sci. Technol.* **2000**, *19*, 205.

10.1021/cm061556+ CCC: $33.50
Published on Web 11/09/2006

currents.[13,17,18] Fluorine-containing precursors were shown, early after the discovery of high-temperature superconductors (HTS), to avoid the formation of $BaCO_3$ as an intermediate reagent, thus allowing growth of HTS at reduced temperature.[19] Unfortunately, the TFA-MOD route for YBCO film growth has as an important drawback the need of a two-step processing, metal-organic pyrolysis leading to amorphous or nanocrystalline intermediate phases and epitaxial oxide film growth, both of them involving complex film transformations. Particularly, the pyrolysis process of TFA precursors for YBCO superconducting films is still poorly understood and hence nonoptimized thermal processes have been traditionally used.[11,13,18,20,21] The challenge is to define a fast thermal process that keeps film homogeneity from the molecular to the macroscopic scales. Usually the removal of the organic constituents in CSD films generates very high film shrinkages due to densification, and hence the film thickness is reduced accordingly.[22] However, the hindrance associated with the substrate during the viscous flow of the amorphous porous network generates strong tensile stresses parallel to the substrate that can generate macroscopic heterogeneities such as macrocracks or film buckling.[3,23] In this work we show that a new, fast (less than 1 h) pyrolysis process of TFA precursors can be used for YBCO film growth which can be defined based on a deep understanding of the mechanisms controlling the metal-organic solution decomposition process and the corresponding film stress relief. We clearly separate the solution drying gel-sintering regime from the decomposition step and we show that the stress relief during this last step can be closely controlled by a combined tuning of temperature ramps and gas flow rate. We also show that during the gel sintering process the generated stress is below that required to induce film instabilities such as buckling. We identify the nanostructural features resulting from the new pyrolysis process by means of TEM and we show that high critical current densities can be achieved with the new defined process. The implication of our work is that the production rate of long length YBCO coated conductors can be strongly increased, thus allowing transforming of CSD into an industrial competitive process.

II. Experimental Methods

YBCO Precursor Solutions. The preparation of YBCO precursor solutions can be carried out from acetate precursors or by reaction of commercial $YBa_2Cu_3O_7$ powder (yttrium-barium-copper-oxide, SOLVAY) with TFAH (Aldrich 99%), or by dissolution, in an inert atmosphere, of the same powder in an excess of TFAA (Aldrich 99%), a small quantity (5−10%) of TFAH (Aldrich 99%) as catalyst, and distilled acetone (Panreac PA) as solvent. However, as a result of the first two reactions, some water is generated; thus, purification processes are required.[24,25] This drawback is overcome in the third reaction. The mixture of TFA salts ($Ba(TFA)_2$, $Cu(TFA)_2$, and $Y(TFA)_3$) is dissolved in sufficient anhydrous methyl alcohol (Aldrich 99.8%) to give a solution with total metal ion concentration of 1−1.5 M. This solution is kept in sealed vials, in an inert atmosphere. The procedure steps that have to be followed for the synthesis of the precursor TFA solution are detailed elsewhere.[25] The viscosity was measured with a rheometer Haake RheoStress 600 (3.5 ± 0.5 mPa s). The metal stoichiometry was checked by inductively coupled plasma (ICP) analysis and the water content has been evaluated by the Karl Fischer method. In this study, two types of YBCO-TFA precursor solutions are used, one with a H_2O content of 0.7 wt % and another with a H_2O content below 10^{-2} wt %. Both of them had a metallic ratio within the range (Y:Ba:Cu) $1:(2 \pm 0.05):(3 \pm 0.05)$.

Sample Preparation. Film deposition on 5 mm × 5 mm $LaAlO_3$ (100) single-crystal substrates is performed by spin coating at a typical rotation speed of 6000 rpm and an acceleration of 6000 rpm s^{-1}. The pyrolysis of the precursor films was always carried out in a humid oxygen atmosphere to avoid sublimation of $Cu(TFA)_2$. The temperature ramps and gas flow rates have been modified in an extended range as indicated in the text to investigate their influence on the film morphology, microstructure, and properties (mechanical and superconducting). The pyrolyzed films were grown using a temperature ramp of 1500 °C h^{-1} up to 795 °C with a high-temperature hold of 180 min under a humid nitrogen gas mixed with 200 ppm oxygen, following by an oxygenation process at 450 °C for 5 h.

Instrumentation and Measurements. *Optical Microscopy.* Optical microscopy (OM) was performed on a Nikon Labophot microscope. It has been used to verify the surface quality of the precursor films after pyrolysis.

Atomic Force Microscopy. The detailed study of the microstructure of the layers after low-temperature decomposition has been carried out by atomic force microscopy (AFM) on a PicoSPM from Molecular Imaging. Scans of 20 μm × 20 μm and 2 μm × 2 μm areas have been typically obtained in a contact mode.

Scanning Electron Microscopy. Scanning electron microscopy (SEM) was realized on a Philips-SEM 515. It has been used to characterize the surface morphology of the final YBCO films.

Transmission Electron Microscopy. Cross-sectional transmission electron microscopy (XTEM) has been performed using a Jeol 2010 FEG electron microscope operated at 200 kV (point-to-point resolution 0.19 nm) equipped with a Gatan Image Filter 2000 EELS spectrometer with an energy resolution of 0.8 eV. Thin foils for XTEM observation were prepared by the conventional cutting, gluing, and grinding procedures, followed by a final milling step with Ar ions down to perforation.

X-ray Diffraction. X-ray diffraction (XRD) has been used to ascertain the phase purity and to determine the texture quality of the final YBCO films. It was carried out using a Rigaku diffractometer. It has a focused monochromatic Cu $K\alpha_1$ rotated source with radiation $\lambda = 1.54$ Å.

TGA−DTA. The used equipment for our TGA and DTA studies is a thermo balance TGA851LF from Metller Toledo, based on a platinum-rhodium resistance furnace which has a maximum temperature of 1600 °C. The maximum weight that can be measured

(17) McIntyre, P. C.; Cima, M. J.; Smith, J. A., Jr.; Hallock, R. B. *J. Appl. Phys.* **1992**, *71*, 1868.
(18) Obradors, X.; Puig, T.; Pomar, A.; Sandiumenge, F.; Mestres, N. *Studies of High Temperature Superconductors*; Narlikar, A., Ed.; Nova Science Publishers: New York, 2005; Vol. 49, p 79.
(19) Gupta, A.; Jagannathan, R.; Cooper, E. I.; Giess, E. A.; Landman, J. I.; Hussey, B. W. *Appl. Phys. Lett.* **1988**, *52*, 2077.
(20) Araki, T.; Kato, T.; Muroga, T.; Niwa, T.; Yuasa, T.; Kurosaki, H.; Iijima, Y.; Yamada, Y.; Hirayama, T.; Saitoh, T.; Shiohara, Y.; Hirabayashi, I. *IEEE Trans. Appl. Supercond.* **2003**, *13*, 2803.
(21) Araki, T.; Hirabayashi, I. *Supercond. Sci. Technol.* **2003**, *16*, R71.
(22) Scherer, G. W. *J. Sol-Gel Sci. Technol.* **1997**, *8*, 353.
(23) Dawley, J. T.; Clem, P. G.; Siegal, M. P.; Tallant, D. R.; Overmyer, D. L. *J. Mater. Res.* **2002**, *17*, 1900.
(24) Obradors, X.; Puig, T.; Pomar, A.; Sandiumenge, F.; Piñol, S.; Mestres, N.; Castaño, O.; Coll, M.; Cavallaro, A.; Palau, A.; Gazquez, J.; Gonzalez, J. C.; Gutierrez, J.; Roma, N.; Ricart, S.; Moreto, J. M.; Rossell, M. D.; van Tendeloo, G. *Supercond. Sci. Technol.* **2004**, *17*, 1055.
(25) Roma, N.; Morlens, S.; Ricart, S.; Zalamova, K.; Moreto, J. M.; Pomar, A.; Puig, T.; Obradors, X. *Supercond. Sci. Technol.* **2006**, *19*, 521.

is 1 g with a resolution of 1 μg. The purity of the used gases is higher than 5 ppm.

Infrared Spectroscopy (IR). The decomposition of the TFA precursors could be easily determined through identification of the absorption line in the FT-IR spectra due to the carboxyl group in films heated at different temperatures. The study has been realized on a Spectrum One FT-IR spectrometer from Perkin-Elmer Instruments. The data was collected over the total range of 2000−500 cm^{-1} with resolution of 4 cm^{-1}.

μ-Raman Spectroscopy. Micro-Raman measurements were carried out using the 5145 Å line of an argon-ion laser at room temperature with a Jovin-Yvon T-64000 Raman spectrometer attached to an Olympus microscope and equipped with a liquid-nitrogen-cooled CCD detector. The used laser spot size on the sample was ~1 μm. Raman spectra were recorded in backscattering geometry. The laser power onto the sample was kept below ~10 $kW \cdot cm^{-2}$ to avoid degradation on the films due to overheating of the proved volume.

Thickness Measurements. The film thickness was measured with a profilometer (Nanopics 2100 from KLA-Tencor). All grown samples are ≈300 nm thick.

Nanoindentation Measurements. A commercial Nano Indenter system (MTS System with TestWorks4 software) was used following a continuous stiffness measurement technique using a diamond Berkovich triangular pyramidal tip indenter (tip B2252-LFM with 15−20 nm diameter) at a frequency of 45 Hz. A value of Poisson's ratio $\nu = 0.18$ was used. The contact stiffness S (N m^{-1}), elastic modulus (Young's modulus) E (GPa), and hardness H (GPa) were determined as a function of nanoindentation contact depth from these measurements. At least 10 load−penetration curves were recorded for each film to ensure the determination of reliable mechanical parameters.

Conductivity and Critical Current Measurements. Electrical resistivity was obtained using the four-point technique and inductive critical current density (J_c) measurements were performed on a SQUID magnetometer (Quantum Design, MPMS-XL).

III. Results and Discussion

The main difficulty in achieving homogeneous films prepared by CSD is to know precisely which parameters control the different stages of densification to reach smooth film shrinkage during the drying, sintering, and decomposition processes.[2,3,22,26] TGA−DTA analysis allows first the knowledge at which temperatures the endothermic drying process and the exothermic pyrolysis process occur. Early works suggested that TFA precursors for YBCO growth decompose within the 200−250 °C temperature range.[21] More recent works, however, have shown that the TFA precursors decompose mainly in the range 250−320 °C; however, some weight loss is already detected below 250 °C[25,27] without having identified its origin. Hence, it is necessary to investigate all the solution and film transformation processes occurring from room temperature up to the completion of the pyrolysis to understand the formation of epitaxial YBCO films. Most investigations of the pyrolysis process of metal-organic precursors for thin film preparation have concentrated on the influence of heating profiles as a means of controlling the decomposition process. However,

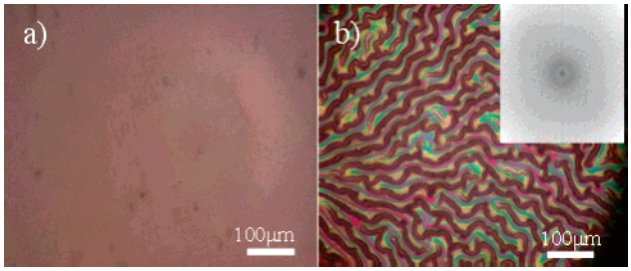

Figure 1. Polarized optical microscopy images of two films heated with a ramp of 300 °C h^{-1} up to (a) 250 °C and (b) 310 °C. Both films were quenched to room temperature after achieving the corresponding maximum temperature. The linear gas flow during these experiments was 2.2 mm s^{-1} and the TFA solution had a water content of 0.7 wt %. Inset of (b): fast Fourier transformation (FFT) of the main image showing that the periodicity of the buckled structure is periodic with a wavelength $d \approx 6.3$ μm.

the pyrolysis of the metal-organics involves a solid−gas exchange of chemical species and hence the external gas flow can become an additional parameter to control the kinetics. The influence of this parameter in the pyrolysis of TFA precursors for YBCO has not been reported up to now, while as will be shown below, it is highly relevant. The exact nature of the chemical reactions involved in the decomposition of the TFA precursors is not known, but early reports have schematized it as follows:[19,28−30]

$$Cu(TFA)_2 + 2Ba(TFA)_2 + 3Y(TFA)_3 + H_2O + O_2 \rightarrow CuO + Ba_{1-x}Y_xF_{2+x} + Y_2O_3 + \text{volatile products} \quad (1)$$

The composition of the solid solution Ba−Y fluoride, however, is still not clearly established.[31] The remaining Y ions probably are incorporated in an amorphous matrix because no crystalline Y_2O_3 phase could be identified by either X-ray diffraction, electron diffraction, or μ-Raman spectroscopy.[32] Finally, up to now, the identified volatile products are CO_2 and HF, but the formation of fluorocarbons cannot be disregarded. It is clear, in any case, that the advancement of the reaction requires the elimination of exhausting gases and hence the reaction kinetics can also be controlled by the external gas flow.

We have first analyzed the macroscopic homogeneity of the films and its relationship with their mechanical properties at different transformation stages by means of optical microscopy (OM), atomic force microscopy (AFM), and nanoindentation, and in a second stage, more microscopic analysis of the films have been carried out by means of SEM and TEM that have been correlated with the superconducting properties of the YBCO epitaxial films.

Film Morphology. Figures 1a and 1b show typical OM images of films quenched from 250 and 310 °C, respectively,

(26) Brinker, C. J.; Scherer, G. W. *Sol-Gel Science: The Physics and Chemistry of Sol- Gel Processing*; Elsevier Science: New York, 1989.
(27) Dawley, J. T.; Clem, P. G.; Boyle, T. J.; Ottley, L. M.; Overmyer, D. L.; Siegal, M. P. *Physica C* **2004**, *402*, 143.
(28) Yoshizumi, M.; Seleznev, I.; Cima, M. J. *Physica C* **2004**, *403*, 191.
(29) Tokunaga, Y.; Fuji, H.; Teranishi, R.; Matsuda, J.; Asada, S.; Kaneko, A.; Honjo, T.; Izumi, T.; Shiohara, Y.; Yamada, Y.; Murata, K.; Iijima, Y.; Satoh, T.; Goto, T.; Yoshinaka, A.; Yajima, A. *Physica C* **2004**, *412−414*, 910.
(30) Shibata, J.; Honjo, T.; Fuji, H.; Araki, T.; Hirabayashi, I.; Hirayama, T.; Izumi, T.; Shiohara, Y.; Yamamoto, T.; Ikuhara, Y. *J. Mater. Res.* **2002**, *17*, 1266.
(31) Matsuda, J. S.; Tokunaga, Y.; Nakaoka, K.; Teranishi, R.; Aoki, Y.; Fuji, H.; Yajima, A.; Yamada, Y.; Izumi, T.; Shiohara, Y. *Physica C* **2005**, *426−431*, 1051.
(32) Gazquez, J.; Sandiumenge, F; Coll, M.; Pomar, A.; Mestres, N.; Puig, T.; Obradors, X.; Kihn, M.; Casanove, M. S.; Ballesteros, C. (to be published).

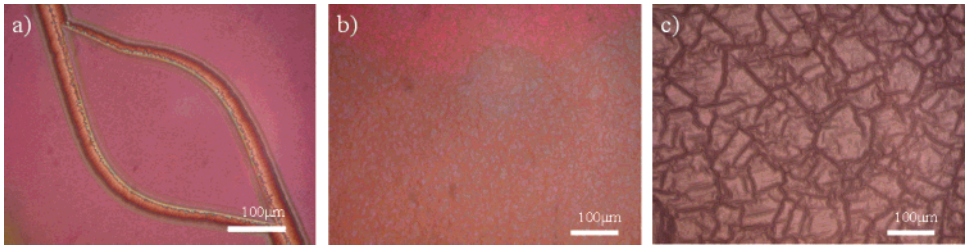

Figure 2. Polarized optical microscopy images of films pyrolyzed with different heating ramps in the 250−310 °C temperature range under a linear gas flow of 2.2 mm s^{-1}. The corresponding heating ramps were as follows: (a) 3 °C h^{-1}, (b) 300 °C h^{-1}, and (c) 900 °C h^{-1}. Similar film morphologies were found under these conditions when TFA solutions with different water contents were used (0.7 wt % and anhydrous).

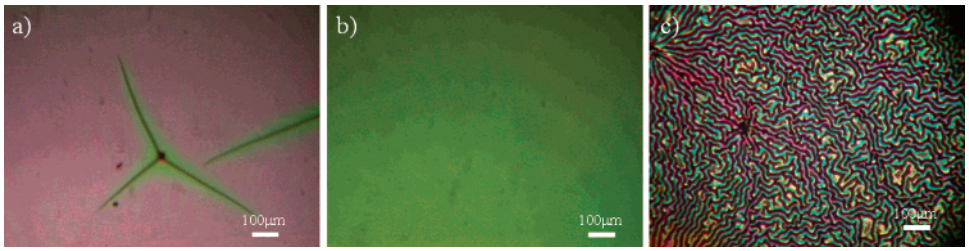

Figure 3. Polarized optical microscopy images of pyrolyzed YBCO films after heating in the temperature interval 250−310 °C with different gas flows. All the films were heated at 300 °C h^{-1} while the linear gas flow was the following: (a) 0.9 mm s^{-1}, (b) 2.2 mm s^{-1}, and (c) 22 mm s^{-1}. Similar film morphologies were found under these conditions when TFA solutions with different water contents were used (0.7 wt % and anhydrous).

after heating the films to these temperatures at 300 °C h^{-1}. These images display two characteristic behaviors for the film transformation which appear to be strongly dependent on external parameters such as heating rate, maximum temperature, and gas flow. As can be appreciated, the film appears very homogeneous when the maximum temperature was 250 °C while after heating it up to 310 °C the film displays a surface-buckled structure. The microscopic origin of this buckled structure, and its consequences on the superconducting performances of the films, will be further discussed, but at this stage we can clearly conclude that nonhomogeneous films may be generated in a fast heating process up to 310 °C. We have then separately investigated the film behavior below 250 °C, where as will be shown later, very little advancement of the pyrolysis occurs, and in the temperature range 250−310 °C, where most of the metal-organic decomposition occurs. A wide range of heating rates were investigated at temperatures below 250 °C, from 300 °C h^{-1} up to 1500 °C h^{-1}, while the oxygen linear gas flow was kept within the range 0−4.5 mm s^{-1}. It was found that when the heating rate was kept at 300 °C h^{-1}, all the films preserved a homogeneous morphology, whatever gas flow was used. At higher heating rates, instead, it was found that the two TFA solutions, having different water contents, led to films with modified qualities. While the anhydrous TFA-MOD films could be treated up to 1500 °C h^{-1} under a gas flow of 3 mm s^{-1}, the films prepared with solutions having some water residues (0.7 wt %) typically showed some buckling at this thermal heating rate.

In a second stage we investigated the influence of the annealing conditions of the films in the range 250−310 °C, after heating them at 300 °C h^{-1} from room temperature up to 250 °C. Figures 2a−2c, on one hand, display OM images of films where the influence of the heating rate on the film homogeneity can be discerned for a given value of the linear gas flow. Figures 3a−3c, on the other hand, show the evolution of the film homogeneity with the linear gas flow

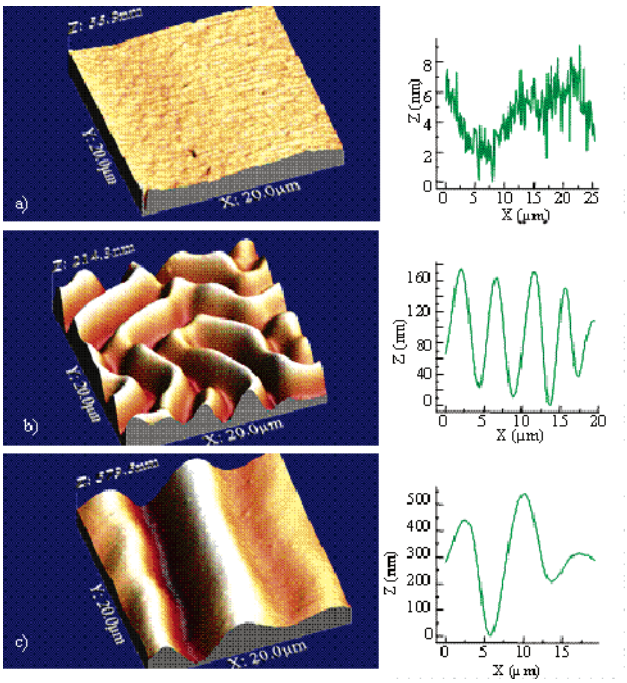

Figure 4. AFM images and height profiles of three YBCO films treated at 250 °C under a linear gas flow of 2.2 mm s^{-1} and having three different characteristic surface finishings due to the differences in temperature ramps: (a) smooth surface (300 °C h^{-1}), (b) buckled surface (1500 °C h^{-1}), and (c) cracked surface (1500 °C h^{-1}).

for a single heating rate. In both cases it may be concluded that there are optimal heating rates and linear gas flows. When one of these variables is too high, the films appear, either buckled or with macrocracks. On the other hand, if either the heating rate or the gas flow is too small, mainly macrocraks may develop.

AFM images of the three characteristic surfaces finishing of the films may give further insight on the morphology of the pyrolyzed films. Figures 4a−4c show AFM images obtained in a typical homogeneous film, a buckled film, and one that has developed a macrocrack. Note the different

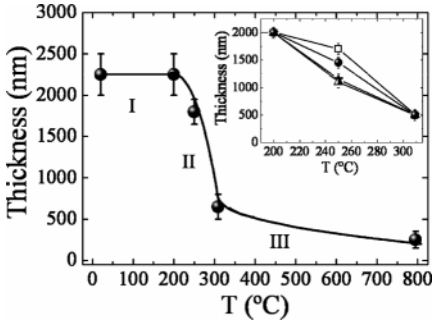

Figure 5. Film thickness evolution with annealing temperature when a heating rate of 300 °C h^{-1} and a gas flow of 2.2 mm s^{-1} are used. Three regions can be identified: region I where the thickness remains constant or slightly reduced, region II where the most significant film shrinkage occurs, and region III where the porous pyrolyzed film is transformed to an epitaxial film. Inset: Detail of the influence of the heating ramp and the gas flow on the film thickness evolution within region II. The data represented in the inset corresponds to a heating rate of 300 °C h^{-1} (●) and 1500 °C h^{-1} (▲, □); the linear gas flow rates are indicated as 0.9 mm s^{-1} (□) and 3 mm s^{-1} (▲, ●).

vertical scales of the line profiles included in these figures. While a smooth film has a typical roughness of a few nanometers, a buckled structure can have surface wrinkles in excess of 150 nm and a macrocrack can be as deep as 500 nm. As we will see later, the typical film thickness after pyrolysis is ∼500 nm; therefore, the observed macrocracks cross the entire films, which is what usually happens in CSD films.[3,33]

The exact mechanism for the formation of buckling in the TFA-MOD YBCO films is still not known.[23] Some clues can be obtained, however, if we investigate the influence of the above-mentioned thermal treatments and gas flows on the evolution of the film thickness. Figure 5 shows the dependence of the film thickness, as measured with a profilometer, on the heating temperature when a single heating rate (300 °C h^{-1}) and linear gas flow (2.2 mm s^{-1}) is used. Three different regions can be loosely identified. In region I the film thickness is not modified or just slightly reduced, independently of the heating rate and the gas flow. In region II a large decrease of the film thickness occurs. The inset of the Figure 5 amplifies the thickness evolution in this intermediate temperature range (region II) where some dependence of the film thickness on the linear gas flow and the heating rate during the pyrolysis is detected. Finally, region III corresponds to the evolution of the film thickness from the pyrolyzed state to a full film epitaxy. The film transformation in this region is quite complex and it will be further analyzed elsewhere.[32]

As can be observed in the inset of Figure 5, when fast heating rates or low gas flow rates are used, the film shrinkage is reduced in region II. The origin of this phenomenon appears to be complex, however, and its understanding requires determining if some sintering of the gelified TFA films occurs and the degree of advancement of the decomposition of the TFA precursors leading to densification of the films. To investigate these matters, we performed a TGA−DTA analysis of the TFA solutions (Figure 6a) and we recorded FTIR spectra of the films

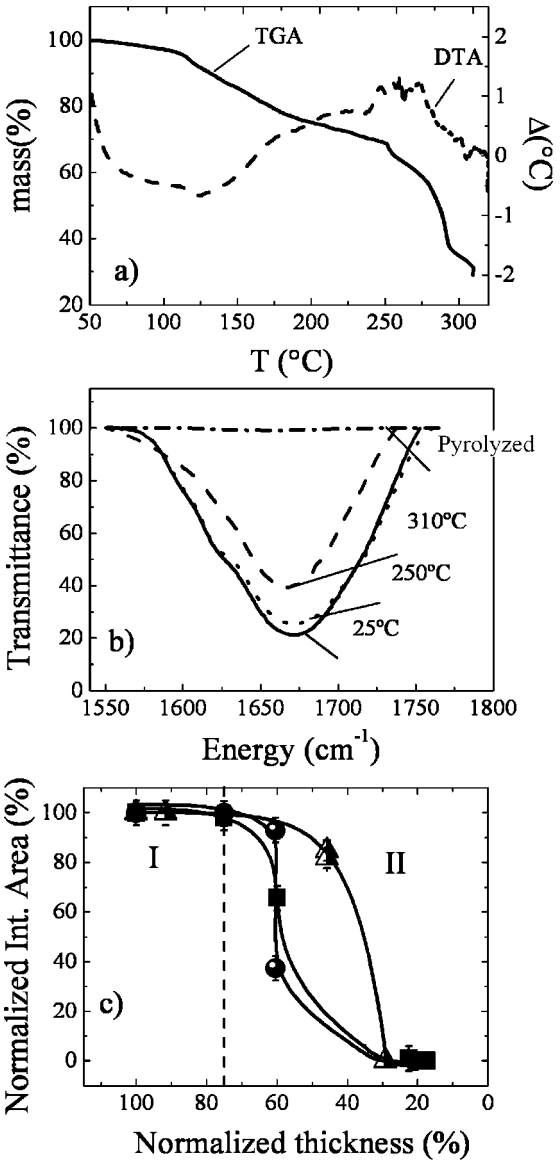

Figure 6. (a) TGA/DTA record of an anhydrous TFA solution when a heating ramp of 30 °C h^{-1} is used; (b) detail of FTIR spectra of a TFA film after deposition where the absorption peak of the carboxyl group is identified (1668 cm^{-1}); (c) representation of the evolution of the normalized intensity of the IR peak corresponding to the carboxyl group versus the normalized film thickness when the films are heated at different temperatures under different conditions. The data represented in (c) correspond to a heating rate of 300 °C h^{-1} (●) and 1500 °C h^{-1} (▲, ■). The linear gas flow rates are indicated as 0.9 mm s^{-1} (■) and 3 mm s^{-1} (▲, ●).

(Figure 6b) following several thermal annealings under well-specified conditions. As can be seen in the FTIR spectra of the as-deposited TFA films, the carboxyl group of the TFA salts can be easily discerned and hence the degree of advancement of the decomposition reaction can be quantified. When the evolution of the intensity of the carboxyl group absorption peak is compared to the evolution of the corresponding film thickness, we can discern if the film shrinkage is associated with a sintering process of the gelified films (i.e., when the TFA precursors still have not been decomposed) or to a densification process associated with the TFA precursors decomposition. Figure 6c displays the relationship between the FTIR intensity of the carboxyl group and the corresponding film thickness reduction. From this figure we can identify region I (below ∼200−250 °C) as that where

(33) Clem, P. G.; Jeon, N. L.; Nuzzo, R. G.; Payne, D. A. *J. Am. Ceram. Soc.* **1997**, *80*, 2821.

no decomposition of TFA occurs while the film thickness is already reduced (by as much as 20%) together with some weight loss, as measured by TGA, also as high as ~20%. These features indicate that in this region a drying−sintering process of the gel occurs where the molecular film network becomes more compact. As was previously discussed by Araki and Hirabayashi[21] and Roma et al.,[25] TFA solutions may trap alcohols or water from the solvent; therefore, our analysis shows that these impurities are evaporated during this first heating stage and the elimination of intermolecular alcohols induces a sintering process of the TFA gel network driven by the capillary forces.

Within region II very different film states can be achieved depending on the heating rate and external gas flow rate. The final heating temperature used in the pyrolysis (310 °C) leads to a film with a thickness 30% of the initial one but this state can be reached through different paths (Figure 6c). For instance, a fast heating rate (1500 °C h^{-1}) combined with a high gas flow (3 mm s^{-1}) generates a film with a thickness 40% of the initial one with only 20% advancement of the decomposition reaction. On the other hand, a slow heating rate (300 °C h^{-1}) combined with the same gas flow (3 mm s^{-1}) has decomposed 60% of the precursors but the film thickness is still 60% of the initial one. Overall, our results indicate that the advancement of reaction (1) occurring within region II can be tuned by the external gas flow and the heating ramp through a viscoelastic process. In all cases, nevertheless, the final film thickness after completing the decomposition reaction of the trifluoroacetates was found to be the same, i.e., ~30% of the initial one. Overall, it seems very understandable that the deep chemical and microstructural rearrangements occurring in the narrow temperature range identified as region II can strongly influence the final properties of the YBCO films and hence an investigation of the evolution of the nanomechanical properties of the films during these transformations would be very useful.

Nanomechanical Properties. Film shrinkage in CSD always leads to a tensile stress parallel to the substrate because an adherent film cannot contract in the plane parallel to the substrate while a viscous flow can easily occur perpendicular to the substrate. This tensile stress parallel to the substrate generated by the film shrinkage seems to be easily accommodated by the TFA gel network before its decomposition starts (T < 200−250 °C). The tensile stress of the film generated during shrinkage lies at the origin of the observation in some films of a buckled structure or of macrocracks. Apparently, the viscous mass transport associated with the gel to inorganic nanometric-amorphous film transformation occurring within the 250−310 °C temperature range has more difficulty occurring in a film with a reduced compliance and so an enhanced tensile stress is generated that may eventually lead to film buckling or macrocrack formation. These effects will depend on the heating rate and gas flow because the film thickness evolution, and hence the tensile stress, is modified by these parameters controlling the transformation rate of the film. These kinetic effects actually confirm the relevance of the viscoelastic behavior of the resulting inorganic film. In Figure 7 we summarize the conditions (heating rate in the 250−310 °C range and linear gas flow) under which homogeneous films morphologies are observed for the two types of TFA solutions used in this work. As can be appreciated, a wider range of pyrolysis conditions can be used with anhydrous TFA metal-organic solutions. We have found, for instance, that anhydrous solutions are less sensitive to high gas flow rates. Outside the indicated regions in Figure 7 buckled films tend to appear at higher film transformation rates (higher heating ramps and enhanced linear gas flow) and films having macrocracks are more easily formed at reduced transformation rates. As is well-known, a macrocrack can only extend in a film when the film thickness exceeds a critical value

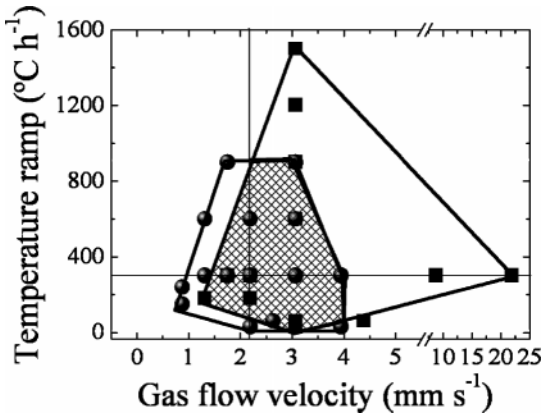

Figure 7. Identification of the heating conditions leading to high-quality pyrolyzed films. The films were heated up to 250 °C at a rate of 300 °C h^{-1} while the temperature annealing ramp in the range 250−310 °C and the linear gas flow were modified. Results for two types of TFA solutions (anhydrous (■) and with 0.7 wt % H_2O (●)) are reported. Hatched zone indicates the region where homogeneous films are obtained for the two types of TFA-YBCO solutions.

$$t_c = \frac{2G_cE}{Z\sigma^2(1-\nu)}$$

where G_c is the energy needed to form two crack surfaces, E is Young's modulus, ν is Poisson's ratio, Z is a dimensionless geometrical parameter, and σ is the biaxial tensile stress of the film.[3] In most of the films investigated here (with final thickness ~ 300 nm) this critical value was not achieved and so no macrocracks were observed. Nevertheless, the tendency to form cracks in films pyrolyzed at low decomposition rates (small heating rates and low gas flow rates) could indicate that the plastic flow existing in these films during the decomposition could enhance the tensile stress and hence the critical value t_c could be exceeded. This point, however, would require further experimental investigation.

The spontaneous generation of complex ordered relief structures has been previously observed in many types of polymeric systems when they are submitted to compressive strains above a critical value.[34−36] The regularity of the wavelength characterizing these buckled structures has even been proposed as a tool for fast determination of polymeric

(34) Borden, N.; Brittain, S.; Evans, A. G.; Hutchinson, J. W.; Whitesides, G. M. *Nature* **1998**, *393*, 146.
(35) Stafford, C. M.; Harrison, C.; Beers, K. L.; Karim, A.; Amis, E. J.; Vanlandingham, M. R.; Kim, H.; Volksen, W.; Miller, R. D.; Simonyl, E. E. *Nat. Mater.* **2004**, *3*, 545.
(36) Volynskii, A. L.; Bazhenov, S.; Lebedeva, O. V.; Bakeev, N. F. *J. Mater. Sci.* **2000**, *35*, 547.

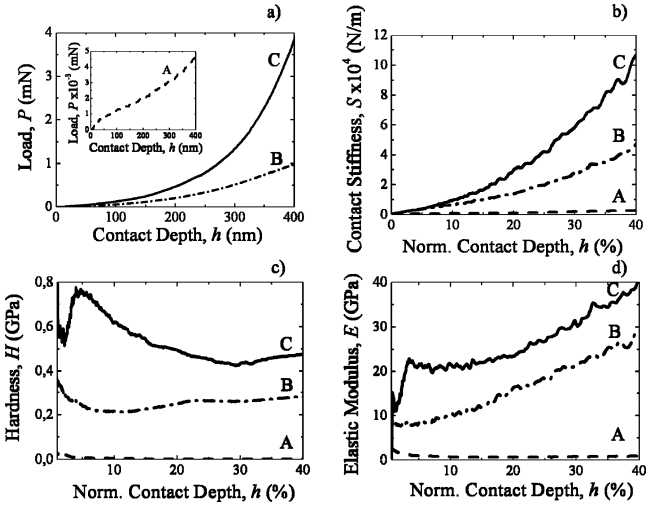

Figure 8. (a) Load−displacement curves recorded for three films at different stages of transformation and thickness reduction: Film A was annealed at 200 °C and it has a thickness ∼75% of the initial one; film B was annealed at 250 °C and it has a thickness that is ∼60% of the initial one; film C was fully pyrolyzed at 310 °C for 30 min and it has a film thickness ∼30% of the initial one. The constant stiffness *S* (b), the hardness *H* (c), and the elastic modulus *E* (d) as a function of the contact depth of the three series of films described above (A, B, and C) are shown. Note that penetration depth has been normalized to the thickness of the corresponding films, as measured with the profilometer.

nanometric film's elastic modulus when they are adhered to a substrate that can be bended in a controlled way.[35] In the YBCO-TFA films investigated here the amplitude of the wrinkles observed in buckled films is about 10% of the total film thickness and the wavelength is of several micrometers with a remarkable regularity, as indicated by fast Fourier transformation (FFT) analysis of the optical images (see the inset of Figure 1b). From these data an estimation of the elastic modulus of the gelified or porous pyrolyzed YBCO films when the buckled structure is created can be obtained from the following equation:[34]

$$\frac{E_f}{(1-\nu_f^2)} = \frac{3E_s}{(1-\nu_s^2)}\left(\frac{d}{2\pi h}\right)^3 \qquad (2)$$

where the subscripts "f" and "s" denote the film and substrate, respectively, h is the film thickness, d is the wavelength of the buckled structure, ν is Poisson's ratio, and E is Young's modulus. If we take into account the E and ν parameters of $LaAlO_3$ single crystals[37] and the observed d values in our films, we can estimate the range of E_f for the different films investigated: $E_f \sim 2-4$ GPa. This Young's modulus should correspond to that of the films at the stage of the pyrolysis process where the buckled structure is initiated. However, due to the strong transformation of the films, we should expect a strong evolution of the mechanical properties of the films. We have therefore investigated the mechanical properties of the gelified and pyrolyzed films directly through nanoindentation measurements. Figure 8a shows typical initial load−displacement curves recorded for three films at different stages of transformation, and so of thickness reduction, as was shown in Figure 5 (all of them heated at 300 °C/h): (1) a partially dried−sintered gelified TFA film annealed at 200 °C (film A), i.e., before any decomposition of the TFA precursors but already displaying some gel sintering (film thickness ∼75% of the initial one); (2) a TFA film annealed at 250 °C where only ∼10% TFA decomposition has occurred but where the film thickness is only ∼60% of the initial one (film B); (3) a fully pyrolyzed film annealed at 310 °C for 30 min with a film thickness only 30% of the initial one (film C).

From the load−displacement curves we can estimate the constant stiffness *S*, Young's modulus *E*, and the hardness *H* of the films[38] and we can analyze their homogeneity by performing experiments as a function of the indenter penetration. Figures 8b, 8c, and 8d show the constant stiffness *S*, the hardness *H*, and the elastic modulus *E* as a function of the contact depth normalized to the film thickness for the three series of films described above.

As can be observed, all three parameters, the stiffness constant *S*, the elastic modulus *E*, and the hardness *H*, are clearly enhanced during the consecutive gel drying−sintering and pyrolysis processes. It is particularly amazing to signal the strong increase of the hardness *H* and Young's modulus *E* of the films after completing the drying and sintering step of the gel network, i.e., when going from film A to B (both *E* and *H* increased by more than a factor of 20). It is also very remarkable that the measured *E* value for film B near the surface ($E \sim 8$ GPa) is in the range of that calculated from eq 2 based on the periodicity of the observed buckled structures in the films. This fact gives consistency to our analysis of the nanomechanical properties of these films. We would like to mention at this point that direct stress measurements of YBCO-TFA films[39] have shown that a maximum stress ($\sigma \sim 70$ MPa) is achieved in the films within the temperature window 250−300 °C, though the exact temperature could depend on the heating profile and so more detailed measurements would be required.

Figures 8b, 8c, and 8d also show that films B and C display some enhancement of the constant stiffness *S* and the elastic modulus *E* when the contact depth is increased. This effect has been previously observed in multilayered magnetic coatings displaying viscoelastic properties[38] and it could indicate that the films have a graded structure, for instance, a decrease of the film porosity, when approaching the interface with the substrate.[35] Similarly, a systematic increase of ∼50% in the estimated elastic modulus *E* has been observed in buckled films when the load−displacement curve is measured on top of the wrinkles, as compared to the valleys. This could indicate again a slight gradient of the film compactness associated with the surface wrinkles.

Finally, we would just signal that the mechanical properties of the epitaxial YBCO films obtained after high-temperature growth were found by nanoindentation to be $H = 3$ GPa and $E = 80$ GPa. This is a very significant enhancement (∼400−500%) of the mechanical properties, as compared to the porous pyrolyzed films, in agreement with the nearly 100% density achieved after the growth process for epitaxial films.[13,24,40]

(37) Harrison, R. J.; Redfern, S. A. T. *Phys. Earth Planet. Interiors* **2002**, *134*, 253.
(38) Li, X.; Bhushan, B. *Mater. Charact.* **2002**, *48*, 11.
(39) Clem, P. G. Private communication.

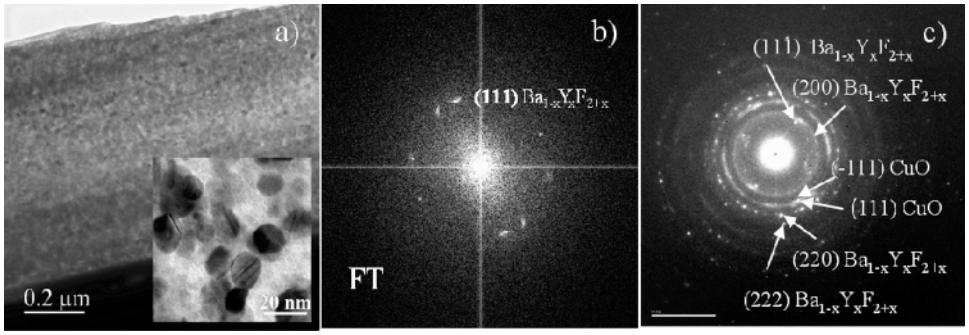

Figure 9. (a) Low-magnification XTEM image of the pyrolyzed film observed from [100] LAO. The precursor forms a homogeneous, ~800 nm thick film. Inset: Higher resolution XTEM image showing a film composed of nanoparticles with a size of ~10−20 nm embedded in an amorphous matrix. (b) Fourier transformation and (c) selected-area diffraction patterns from an area containing the precursor layer where the identified phases are indicated.

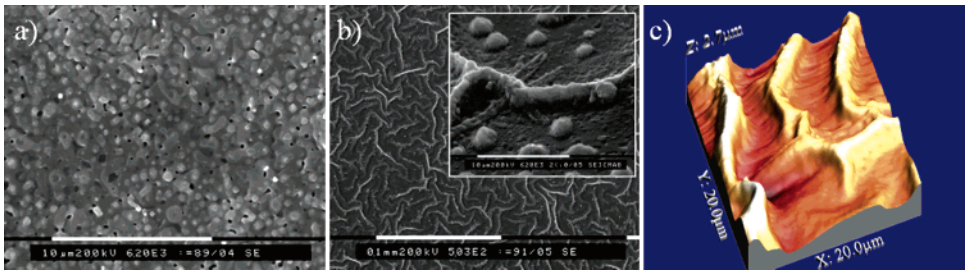

Figure 10. (a) Typical SEM image of a homogeneous YBCO film after high-temperature growth. Note that a low-porosity film is achieved. (b) SEM image of a YBCO film after the growth stage and display of buckling after the pyrolysis process. A detail of the ripple is shown in the inset. (c) AFM image of the YBCO film shown in (b). The height of the wrinkles was estimated to be ~100 nm.

Summarizing, we have shown that very significant mechanical transformations of the films occur during the three identified stages, drying and sintering of the TFA gel molecular network, densification associated with the gel network disruption, and finally, film crystallization leading to a dense epitaxial structure.

Film Microstructure and Superconducting Properties. TEM and electron diffraction analysis of pyrolyzed films, i.e., heated at 310 °C and signalling the origin of region III in Figure 5, were carried out to investigate the film structure at the nanometric scale, to identify the crystalline phases formed, and to ascertain if the film homogeneity is preserved. Figure 9a displays a low-magnification TEM cross-section image where the whole thickness of a fully pyrolyzed film is observed. A homogeneous pore structure is seen, although some increase of the density when approaching the substrate, as was suggested by nanoindentation experiments, cannot be disregarded. The total thickness of the film agrees with that typically observed after completion of the film pyrolysis (Figure 5a). A higher magnification TEM image is shown in the inset of Figure 9a. This image shows that nanometer scale (~10−20 nm) quasi-spherical particles are formed embedded in a quasi-amorphous matrix. Fourier transformation and selected area electron diffraction were carried out, as is indicated in Figures 9b and 9c where the diffraction pattern is indexed. These diffraction patterns could be fully indexed on the basis of only two randomly oriented crystalline phases: CuO and the solid solution $Ba_{1-x}Y_xF_{2+x}$ in agreement with the decomposition reaction (1). Therefore, we believe that the spherical particles observed in the inset of Figure 9a correspond to CuO while $Ba_{1-x}Y_xF_{2+x}$ nanocrystals remain in the quasi-amorphous matrix. We note that the identification of these phases agree with X-ray diffraction patterns and μ-Raman spectra that could not allow identification of any other phase, particularly Y_2O_3.[32] We could not properly quantify the Y content in the nanocrystalline fluoride phase; however, it seems very likely that most of the Y content in the pyrolyzed films is within this phase. It is also worth noting that the typical size of the CuO nanoparticles observed in our short (~1.5 h) optimized pyrolysis process is similar to that observed in longer annealing processes (~10−20 h between 200 and 250 °C) previously used by other authors,[21,30,41] though some tendency to a coarsening process was detected after heating at 400 °C for very long times.[21,41]

The transformation of the pyrolyzed TFA-YBCO films within region III (Figure 5) leading to epitaxial YBCO films is a complex process involving the formation and microstructural evolution of several intermediate phases.[11,28,30,42−44] A combined TEM, X-ray diffraction, and μ-Raman investigation of the present fast pyrolyzed films will be reported elsewhere.[32] Here, we would like only to stress how important is the preservation of the structural homogeneity of the pyrolyzed films on achieving high superconducting performances. Figure 10a shows a typical SEM image of a homogeneous film after high-temperature growth while Figure 10b shows SEM images of a YBCO film grown after having generated a buckled structure during the pyrolysis. A detail of the preserved wrinkles at the surface of the films can be seen in the inset of Figure 10b and in the AFM image

(40) Castaño, O.; Cavallaro, A.; Palau, A.; Gonzalez, J. C.; Rossell, M.; Puig, T.; Sandiumenge, F.; Mestres, N.; Piñol, S.; Pomar, A.; Obradors, X. *Supercond. Sci. Technol.* **2003**, *16*, 45.
(41) Araki, T.; Niwa, T.; Yamada, Y.; Hirabayashi, I.; Shibata, J.; Ikuhara, Y.; Kato, K.; Kato, T.; Hirayama, T. *J. Appl. Phys.* **2002**, *92*, 3318.
(42) Smith, J. A.; Cima, M. J.; Sonnenberg, N. *IEEE Trans. Appl. Supercond.* **1999**, *9*, 1531.
(43) Solovyov, V. F.; Wiesmann, H. J.; Wu, L.-J.; Suenaga, M.; Venkataraman, K.; Maroni, V. A. *Physica C* **2004**, *415*, 125.
(44) Wu, L.; Zhu, Y.; Solovyov, V. F.; Wiesmann, H. J.; Moodenbaugh, A. R.; Sabatini, R. L.; Suenaga, M. *J. Mater. Res.* **2001**, *16*, 2869.

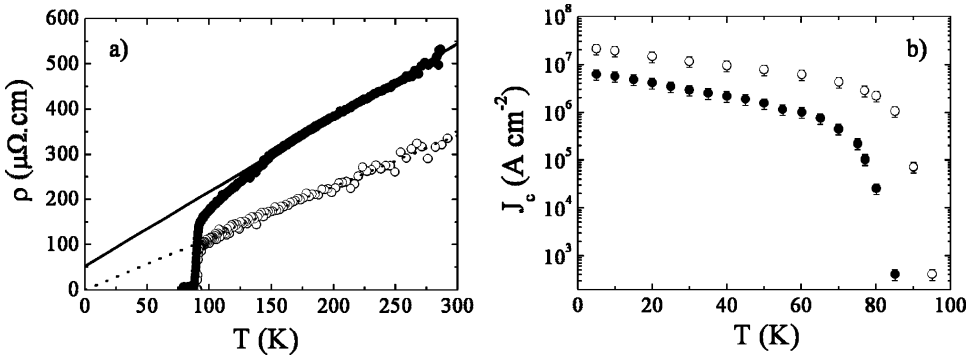

Figure 11. Influence of the film morphology on the physical properties of the YBCO films. Two typical YBCO films grown after pyrolysis processes and leading to smooth (○) and buckled (●) films have been selected to illustrate the general behavior. (a) Temperature dependence of normal state resistivity; (b) temperature dependence of the critical current density.

shown in Figure 10c. It is clear from these images that when a network of surface wrinkles develop during the pyrolysis process, it remains after high-temperature growth. The heights of the measured wrinkles appear to be quite similar to those observed after pyrolysis, i.e., ∼100 nm, and therefore they should have a strong influence on the overall transport properties of the films (thickness of ∼300 nm in the present case). It is not clear which structural rearrangements occur associated with these wrinkles. Actually, X-ray diffraction patterns ($\theta-2\theta$, ω, or ϕ scans) of homogeneous and buckled YBCO films could not signal any structural difference among both films, except a slight decrease of the intensity of the (00l) Bragg lines in the $\theta-2\theta$ patterns. On the other hand, measurements of the temperature dependence of the electrical resistivity in the normal state of YBCO films (Figure 11a) and the temperature dependence of the critical current density in the superconducting state (Figure 11b) clearly showed that some degradation of the transport properties occurs associated with these structural inhomogeneties. Figure 11a shows that T_c is very similar in both types of films; however, slope A of the linear temperature dependence of the resistivity of YBCO films ($\rho(T) = \rho_o + AT$) is increased in buckled films and, additionally, a finite extrapolated 0 K resistivity ρ_o is observed, which indicates that some degradation of the intergrain electrical connectivity occurs. It is very likely therefore that a certain degree of crystalline orientation randomness and porosity is developed in the surface wrinkles of the buckled YBCO films, which increases the normal state resistivity and decreases the critical current density in the superconducting state. To clarify this point, we performed a μ-Raman spectrometry study to identify the microstructural inhomogeneities associated with the wrinkles. Figure 12 shows μ-Raman spectra measured at different points of the buckled sample with a laser spot size diameter of 1 μm. The spectra measured in the "valley" regions of the film surface (see spectrum (a)) display the typical signature of a YBCO film with the *c*-axis perpendicular to the substrate plane: the O(2,3) Raman mode intensity is much stronger than the O(4) intensity.[45] In contrast, the spectra measured at the "hills" of the surface film (see spectra (b) and (c)) show the presence of intermediate or segregated phases like CuO and barium cuprates (Ba−Cu−O) in the 590−650 cm^{-1} range.[46] The larger spectral

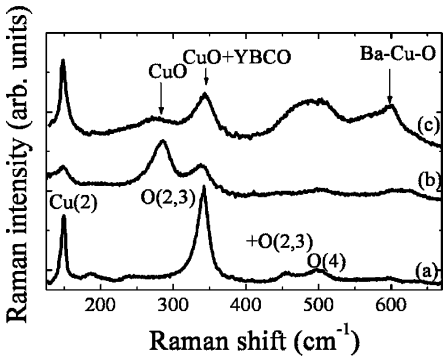

Figure 12. μ-Raman spectra of a buckled YBCO film measured at the (a) "valley" and (b, c) "hill" regions of the film surface, showing the YBCO Raman phonons and the presence of impurity phases.

width of the YBCO modes is also an indication of a poorer crystallization. Moreover, in some cases the signature of a film with a large amount of crystallites oriented with their *a/b*-axis perpendicular to the substrate plane (intense O(4) mode) also appears (see spectrum (c)). All these analyses are in good agreement with those of Dawley and co-workers[9] and they confirm the results from the resistivity measurements, and our suggestion for some degree of a crystalline orientation randomness and porosity occurs at the wrinkles.

Actually, in nonbuckled films a universal correlation among film porosity and critical current density in epitaxial YBCO films has been evidenced recently.[40,47] Minimization of the film porosity requires, first, the achievement of homogeneous films after the metal-organic decomposition and, second, optimized high-temperature growth conditions.[48,49] When both requirements are fulfilled, high critical current densities can be achieved in YBCO films grown from trifluoroacetate precursors, i.e., $J_c = 3-4$ MA cm^{-2} at 77 K in zero magnetic field (Figure 11b).

IV. Summary

The complex processes occurring after deposition of trifluoroacetate (TFA) metal-organic precursor solutions for

(45) González, J. C.; Mestres, N.; Puig, T.; Gazquez, J.; Sandiumenge, F.; Obradors, X.; Usoskin, A.; Joos, C.; Freyhardt, H.; Freenstra, R. *Phys. Rev. B* **2004**, *70*, 094525.
(46) Jee, Y-A.; Ma, B.; Maroni, V. A.; Li, M.; Fischnmer, B. L.; Balachandran, U. *Supercond. Sci. Technol.* **2001**, *14*, 285.
(47) Pomar, A.; Coll, M.; Cavallaro, A.; Gázquez, J.; González, J. C.; Mestres, N.; Sandiumenge, F.; Puig, T.; Obradors, X. *J. Mater. Res.* **2006**, *21*, 1106.
(48) Puig, T.; Gonzalez, J. C.; Pomar, A.; Mestres, N.; Castaño, O.; Coll, M.; Gazquez, J.; Sandiumenge, F.; Piñol, S.; Obradors, X. *Supercond. Sci. Technol.* **2005**, *18*, 1141.
(49) Coll, M.; Gázquez, J.; Pomar, A.; Puig, T.; Sandiumenge, F.; Obradors, X. *Phys. Rev. B* **2006**, *73*, 075420.

high-quality epitaxial YBCO thin film growth have been widely investigated using several microstructural and physical characterization tools which have allowed us to identify three different characteristic temperature regions. In the low-temperature region ($T < 200-250$ °C) the TFA gelified films are transformed through a drying−sintering process but the TFA precursors are essentially not decomposed. At this stage the films are mechanically very soft and they can afford very fast heating rates, preserving their homogeneity. In an intermediate temperature region ($T \sim 250-310$ °C) the TFA precursors are decomposed and most of the film shrinkage occurs (final film thickness ∼30% of the initial one) through a viscoelastic process which strongly hardens the film and thus generates a strong in-plane tensile stress. The decomposition reaction advancement can be tuned, within this region, by the temperature ramp and the external gas flow which allows us to achieve smooth stress relief. The range of parameters leading to homogeneous films and high superconducting performances is wider when anhydrous metal-organic precursors are used. When the film shrinkage process is too fast, the films turn out to be buckled and these anomalous structures strongly degrade the film epitaxy and the superconducting properties after high-temperature growth. Overall, understanding the complex microstructural and chemical transformations leading to epitaxial YBCO films from TFA metal-organic solutions has allowed us to strongly reduce the required pyrolysis time for YBCO film production.

Acknowledgment. This work has been financed by the EU within the scope of the projects Solsulet, Super3C, and Hiperchem, by the Spanish CICYT (MAT02-02642 and MAT03-01584), and by the Generalitat de Catalunya (2001-SGR-00336 and CeRMAE). We acknowledge Serveis de Microscopia Electronica, UAB and UB, for the use of the SEM-EDX and TEM facilities and MATGAS for the nanoindentation system. K.Z. and J.G. acknowledge MCyT for Ph.D. fellowships, and A.P. acknowledges the Spanish Ramon y Cajal program.

CM061556+